AMRX Applied Mathematics Research eXpress
Volume 2006, Article ID 25262, Pages 1–25

Intermediate-Asymptotic Structure of a Dewetting Rim with Strong Slip

P. L. Evans, J. R. King, and A. Münch

When a thin viscous liquid film dewets, it typically forms a rim which spreads outwards, leaving behind a growing dry region. We consider the dewetting behavior of a film, when there is strong slip at a liquid-substrate interface. The film can be modeled by two coupled partial differential equations (PDEs) describing the film thickness and velocity. Using asymptotic methods, we describe the structure of the rim as it evolves in time and the rate of dewetting, in the limit of large slip lengths. An inner region emerges, closest to the dewetted region, where surface tension is important; in an outer region, three subregions develop. This asymptotic description is compared with numerical solutions of the full system of PDEs.

1 Introduction

Recently, the dewetting behavior of a thin liquid film on a solid substrate has received considerable attention. Such behavior is important for the preparation of polymer films, for microfluidic devices, and for other applications.

Experiments by Reiter and others [1, 12, 13] involving dewetting films of polystyrene on polydimethylsiloxane-coated silicon show an asymmetric rim shape, and dewetting at various rates. Efforts to explain these observations have focussed on non-Newtonian rheology, such as viscoelasticity, and on slip at the liquid-solid interface. For example, Vilmin and Raphaël [14] invoke viscoelasticity and "residual stresses" to obtain

Received 16 August 2006; Revised 2 November 2006; Accepted 9 November 2006

models which predict slower-than-linear dewetting rates. More recent experiments [2, 3] involve varying the surface at the substrate-liquid interface, without changing the wetting properties. Fetzer and coworkers observed different film profiles: with one substrate there was a very asymmetric ridge (in particular at early stages of the rim retraction) decaying slowly and monotonically on its outer part onto the undisturbed thickness, while for another substrate, the ridge was more symmetric and the decay became oscillatory as the ridge grew. Fetzer et al. [2] explained the change in ridge structure using a lubrication model (the strong slip lubrication model of Münch et al. [11]) with different amounts of slip at this interface for the two films. The occurrence of slip, or apparent slip, in microfluidics was surveyed by Lauga et al. [9].

Here we study the behavior of a mathematical model for the film which assumes strong slip at the substrate. The model describes the film after rupture has occurred, as the film retracts and the contact line recedes outwards. Münch et al. [11] derived a family of model equations governing the film behavior as the effects of slip are increased. The model is restricted to one space dimension. (The issue of transverse instability on a ridge with slippage has been considered by Münch and coworkers [7, 10] and references therein.) The present work is concerned with the strong slip limit, for which the condition imposed at the substrate is not that the velocity is zero there, but rather a relation involving the velocity gradient. An identical model for the strong slip limit, including inertial effects, was obtained by Flitton [4] (who also included gravity) and by Kargupta et al. [5]. The corresponding regime was also identified in a more complicated (poroviscous) context by King and Oliver [8]. (Note that a term $-\Sigma_z^s$ is omitted from the right-hand side of (A.9) there.)

Previous numerical simulations by Münch et al. [11] have revealed some features of the behavior of solutions for this model, based on a large but finite slip parameter, β, which suggest the behavior expected when $\varepsilon = 1/\beta \to 0$. Figure 1.1 shows a typical film profile during dewetting.

This paper begins by presenting the equations describing the evolution of the film (Section 2). We then argue in Section 3 that the film develops into an inner and an outer region, and state the inner and outer problems in Sections 3.1 and 3.2. The outer region is somewhat complicated, and at large times can be subdivided into three subregions. This is explored in Section 4. We are able to confirm this asymptotic structure through numerical simulations of the original system of PDEs (Section 4.3).

At sufficiently large times the above asymptotic description fails, because the inner region "gobbles up" one of the subregions of the outer. This leads to a new asymptotic structure (Section 5). Further changes in structure occur at still larger times. These will form the subject of a follow-on paper currently in preparation.

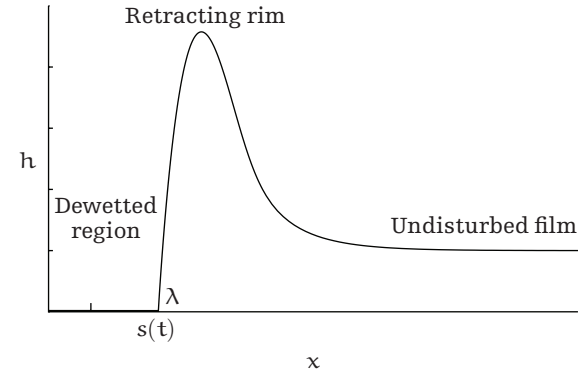

Figure 1.1 Schematic of the dewetting rim.

2 Thin-film model

Here we only briefly summarize the model, as a detailed derivation has previously appeared [11]. The film thickness may vary with position x and time t, and is denoted by $h(x,t)$. Its evolution is governed by the Navier-Stokes equations for momentum and mass conservation of a viscous incompressible liquid, and the stress-strain relationship is assumed to be Newtonian. At the impermeable substrate, the Navier slip boundary condition

$$u = B\frac{\partial u}{\partial y} \tag{2.1}$$

is imposed for the component of velocity tangential to the substrate, u, while the normal component is set to zero. The quantity B is a slip length, with $B = 0$ representing the no-slip case, while $B \to \infty$ represents the limit of perfect slip, where the substrate has no retarding effect on the flow of liquid in the film. The free surface is assumed to be free of tangential stresses, while normal stresses arise from capillarity.

The model is based on the lubrication approximation, which involves expansion in a parameter corresponding to the scale of the free surface slope H/L, (where H and L are typical scales for the film thickness and distance along the substrate, resp.) which is assumed to be small. Neglecting inertia terms, we arrive at the strong-slip model proposed by Münch et al. [11], Flitton [4], and Kargupta et al. [5],

$$\frac{\partial h}{\partial t} + \frac{\partial}{\partial x}(uh) = 0, \tag{2.2a}$$

$$4\frac{\partial}{\partial x}\left(h\frac{\partial u}{\partial x}\right) + h\frac{\partial^3 h}{\partial x^3} = \varepsilon u. \tag{2.2b}$$

Here we have introduced $\varepsilon = 1/\beta$, where $\beta = (HB)/L^2$ is, the dimensionless slip parameter. We consider the strong-slip limit, that is $0 < \varepsilon \ll 1$. (It is also possible to add a term $\widetilde{\delta} h^2 h_{xxx}$ to (2.2b), where $\widetilde{\delta} = (H/L)^2\varepsilon$, to give a "uniformly valid" equation which includes the weak slip limit, in which ε is not small.)

We are concerned with the situation in which the film has already nucleated a dewetted region, so that the free surface meets the substrate at a "contact line," and denote its position by $x = s(t)$. Here $s(t)$ is an unknown function which is to be determined. Equations (2.2) represent dewetting in one dimension, such as when nucleation has occurred along a straight edge, as in experiments by Reiter et al. [13]. For circular dewetting from a hole, they should also be appropriate at sufficiently large dewetted radii. Appropriate boundary conditions for (2.2) at the contact line are

$$h = 0, \qquad \frac{\partial h}{\partial x} = \lambda, \qquad h\frac{\partial u}{\partial x} = 0, \qquad u = \dot{s}(t). \tag{2.3}$$

These represent a requirement for the film to meet the contact line with a contact angle given by $\arctan\lambda$. The third condition corresponds simply to there being no source or sink of momentum at the contact line, other than the net surface tension force at the triple point. The fourth states that the liquid is at rest in a frame moving with the contact line. We remark that the condition $u = \dot{s}(t)$ in fact readily follows from the other conditions. The issue of appropriate boundary conditions for thin films with moving contact lines is considered by King and Bowen [6] and Flitton [4].

In the undisturbed region we impose

$$h \longrightarrow 1, \quad u \longrightarrow 0 \quad \text{as } x \longrightarrow \infty. \tag{2.4}$$

Equations (2.3) and (2.4) provide a total of six boundary conditions.

In the following sections, we will consider the governing equations mostly in a frame of reference that moves with the retracting ridge, that is, in the positive x direction. It is therefore convenient to transform the above equations to a frame of reference having its origin fixed at the contact line, by letting $x = s(t) + x_c$ and $u = \dot{s}(t) + u_c$. This yields, after dropping the subscript "c,"

$$\frac{\partial h}{\partial t} + \frac{\partial}{\partial x}(uh) = 0, \tag{2.5a}$$

$$4\frac{\partial}{\partial x}\left(h\frac{\partial u}{\partial x}\right) + h\frac{\partial^3 h}{\partial x^3} = \varepsilon(\dot{s} + u), \tag{2.5b}$$

and the boundary conditions

$$h = 0, \quad \frac{\partial h}{\partial x} = \lambda, \quad h\frac{\partial u}{\partial x} = 0, \quad u = 0 \quad \text{at } x = 0, \tag{2.6a}$$

$$h \longrightarrow 1, \quad u \longrightarrow -\dot{s} \quad \text{as } x \longrightarrow \infty. \tag{2.6b}$$

As initial data for (2.2), we set

$$s(0) = 0, \qquad h(x,0) = h_{\text{init}}(x) \quad \text{for } x \geq 0, \tag{2.7}$$

where $h_{\text{init}}(x)$ is smooth and positive for $x > 0$ and satisfies the boundary conditions for h in (2.6). Furthermore, we suppose that $h_{\text{init}}(x)$ is a function which makes the transition from $h = 0$ at the contact line to $h \approx 1$ over a region of width $\mathcal{O}(1)$. For example, in some of our numerical simulations we have used the function

$$h_{\text{init}}(x) = \begin{cases} 1 - \left(1 - \dfrac{\lambda}{p}x\right)^p, & 0 < x < \dfrac{p}{\lambda}, \\ 1, & x > \dfrac{p}{\lambda} \end{cases} \tag{2.8}$$

for small values of p, along with other similar initial conditions. The long-time behavior was not found to depend significantly on the details of h_{init}. No initial condition is needed for u as it may be determined from (2.2b) if h is known.

For future reference, we record here the following mass conservation relation which is obtained by integrating (2.5a) by parts and using the boundary and initial conditions,

$$\int_0^\infty \left[h(x,t) - h_{\text{init}}(x)\right] dx = s(t). \tag{2.9}$$

3 Ridge dynamics and profile for $t = \mathcal{O}(1)$, $\varepsilon \to 0$

In the limit $\varepsilon \to 0$ with $t = \mathcal{O}(1)$ the asymptotic structure comprises two regions. These are an inner region, close to the contact line, and an outer region (Figure 3.1). These are considered in turn in the following two sections.

3.1 Inner region

It turns out that in (2.5)-(2.6), the spatial variable x as well as h and u are already scaled appropriately for the inner region. Assuming that $\varepsilon\dot{s} \ll 1$ for t fixed and $\varepsilon \to 0$ (the exact

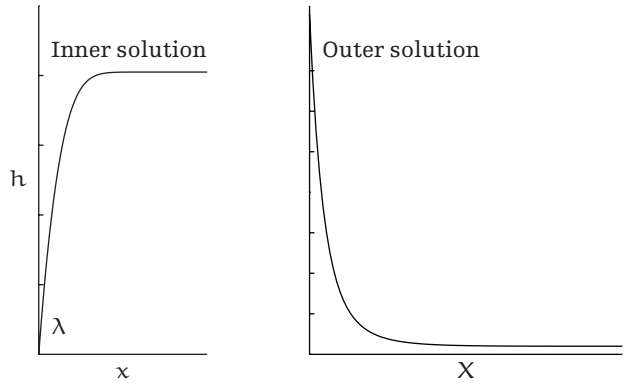

Figure 3.1 Our analysis describes the film as an inner region and an outer region.

behavior for $s(t) = s(t;\varepsilon)$ will be determined in the discussion of the outer region), and expanding $h = h_0 + \mathcal{O}(\varepsilon^{1/2})$ and $u = u_0 + \mathcal{O}(\varepsilon^{1/2})$ in powers of $\varepsilon^{1/2}$, the right-hand side of (2.5b) drops out to leading order. The remaining equation can be integrated once with respect to x, leading to

$$\frac{\partial h_0}{\partial t} + \frac{\partial}{\partial x}(u_0 h_0) = 0, \tag{3.1a}$$

$$4h_0\frac{\partial u_0}{\partial x} + h_0\frac{\partial^2 h_0}{\partial x^2} - \frac{1}{2}\left(\frac{\partial h_0}{\partial x}\right)^2 = -\frac{1}{2}\lambda^2. \tag{3.1b}$$

These evolution equations are supplemented by initial conditions and boundary conditions at $x = 0$,

$$h_0(x,0) = h_{\text{init}}(x) \tag{3.2}$$

$$h_0 = 0, \quad \frac{\partial h_0}{\partial x} = \lambda, \quad h_0\frac{\partial u_0}{\partial x} = 0, \quad u_0 = 0 \quad \text{at } x = 0 \tag{3.3}$$

with (3.3) being used to fix the constant of integration in (2.6a).[1]

[1] We also require that $h_0 h_{0xx} \to 0$ as $x \to 0$, that is, that h_{0xx} be well behaved near $x = 0$; since $h_0 \sim \lambda x$ here, that is indeed the case.

For later matching to the outer solution, we need the behavior of h_0 and u_0 for large x. Probing (3.1) with power law behavior of the form $h_0 \sim H_\infty(t)x^{n_h}$ and $u_0 \sim U_\infty(t)x^{n_u}$, we find that $n_h = 0$ and $n_u = 1$, and hence the far-field behavior of h_0 and u_0 is

$$h_0 \sim H_\infty(t), \quad u_0 \sim U_\infty(t)x \quad \text{as } x \longrightarrow \infty. \tag{3.4a}$$

This form is obtained by seeking self-similar profiles which have h_0 bounded and nonzero for large x. We must therefore have $H_\infty(t)$ and $U_\infty(t)$ satisfying

$$\frac{dH_\infty}{dt} + U_\infty H_\infty = 0, \qquad 4H_\infty U_\infty = -\frac{1}{2}\lambda^2. \tag{3.4b}$$

The behavior of h_{init} at $x \to \infty$ provides us with the initial value $H_\infty(0) = 1$, hence the far-field behavior of h_0 and u_0 is

$$H_\infty(t) = 1 + \frac{\lambda^2}{8}t, \tag{3.4c}$$

$$U_\infty(t) = -\frac{\frac{\lambda^2}{8}}{1+\frac{\lambda^2}{8}}t. \tag{3.4d}$$

The inner problem may be rescaled to remove the parameter λ. This is achieved using the scaling

$$h = \lambda^2 h', \qquad u = \lambda u', \qquad x = \lambda x', \qquad S(t;\varepsilon) = \lambda S'(t;\varepsilon) \tag{3.5}$$

so that the above (3.1) and the boundary conditions at $x = 0$ become independent of λ, with the slope boundary condition there becoming $\partial h/\partial x = 1$. Thus we can consider the case $\lambda = 1$ without loss of generality.

3.2 Outer region

Away from the contact line, we anticipate that the effects of surface tension are unimportant, while the effects of the shear stress at the substrate due to finite slip, that is, the terms on the right-hand side of (2.5b), enter the dominant balance. Accordingly, we define outer variables X and U as follows:

$$x = \varepsilon^{-1/2}X, \qquad h = H, \qquad u = \varepsilon^{-1/2}U, \tag{3.6}$$

and also

$$s(t;\varepsilon) = \varepsilon^{-1/2} S(t;\varepsilon), \tag{3.7}$$

where we assume that U, h, and S are $\mathcal{O}(1)$ for $\varepsilon \to 0$ with t and X fixed. We expand $H = H_0 + o(1)$, $U = U_0 + o(1)$. The function $S = S_0(t) + o(1)$ will be obtained as part of the solution of this outer problem. To leading order, (2.5) becomes

$$\frac{\partial H_0}{\partial t} + \frac{\partial}{\partial X}\left(U_0 H_0\right) = 0, \tag{3.8a}$$

$$4\frac{\partial}{\partial X}\left(H_0 \frac{\partial U_0}{\partial X}\right) = \dot{S}_0 + U_0 \tag{3.8b}$$

for $X > 0$.

This is subject to conditions at $X = S_0$ which are derived from matching to the inner solution. Rewriting (3.4a) in outer variables,

$$H_0 \sim H_\infty(t), \qquad U_0 \sim V_\infty(t) X \quad \text{as } X \longrightarrow 0, \tag{3.9}$$

one obtains the boundary conditions

$$4H_0 \frac{\partial U_0}{\partial X} = -\frac{1}{2}\lambda^2, \quad U_0 = 0 \tag{3.10a}$$

at $X = 0$. The outer problem also needs the far-field boundary conditions derived from (2.6b), namely,

$$H_0 \longrightarrow 1, \qquad U_0 \longrightarrow -\dot{S}_0 \quad \text{as } X \longrightarrow \infty. \tag{3.10b}$$

Initial conditions for H_0 follow by considering the limit of h_{init} in outer variables, and turn out to be trivial, while the initial value for S_0 is just that for s given in (2.7). Summarizing both conditions, we get

$$S_0(0) = 0, \qquad H_0(X,0) = 1 \quad \text{for } X \geq 0. \tag{3.11}$$

Integrating (3.8a) by parts yields the constraint

$$\int_0^\infty \left(H_0 - 1\right) dX = S_0, \tag{3.12}$$

which represents conservation of mass. It could have also been obtained directly from (2.9).

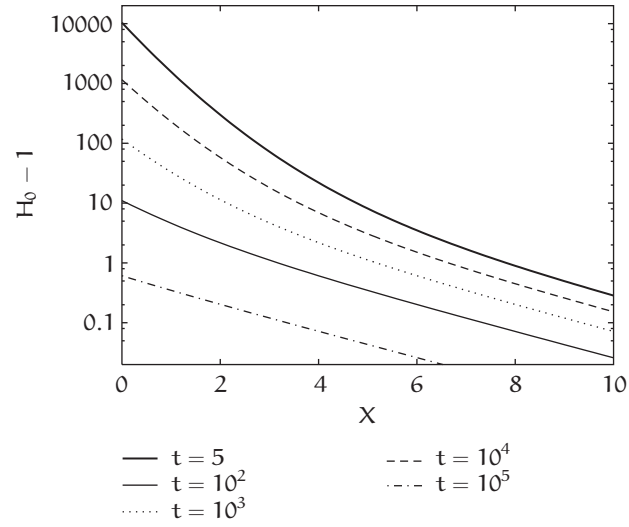

Figure 3.2 Solutions of the outer problem (3.8)–(3.10) at $t = 5$, 100, 10^3, 10^4, and 10^5.

3.3 Composite solution and numerical validation

Equipped with inner and outer solutions, a multiplicative composite solution, uniformly valid in both the inner and outer regions, can be constructed by defining

$$h^{(c)}(x,t) = \frac{h_0(x,t)H_0\left(\varepsilon^{1/2}x,t\right)}{1+\dfrac{\lambda^2 t}{8}}, \tag{3.13a}$$

$$u^{(c)}(x,t) = \frac{-u_0(x,t)U_0\left(\varepsilon^{1/2}x,t\right)}{\dfrac{x}{\left(8/\lambda^2+t\right)}}, \tag{3.13b}$$

where the denominators are the "common parts" given by (3.4).

Next, we compare the full lubrication model solutions to numerical solutions for the inner and outer problems, and to a composite expansion. Throughout, we fix $\lambda = 1$. Details of the Matlab routines used are given in the appendix.

Numerical solutions to the outer problem, (3.8)–(3.11), have been produced. There were 1000 grid points, with a computational domain $0 < X < 50$. Typical thickness profiles are shown in Figure 3.2.

Similarly, numerical solutions to the inner problem, (3.1)–(3.3) and $\partial h/\partial x = 0$ at $x = 20$, starting from (2.8) with $p = 2$ have been computed. These used 200 grid points, with $0 < x < 20$. Figure 3.3 shows profiles at various times, together with the initial condition used. It can be seen that the rim height increases approximately linearly with

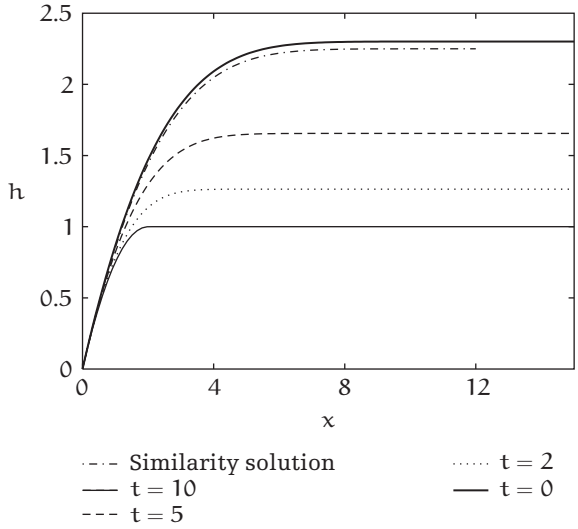

Figure 3.3 Approach of time-dependent solutions of the inner problem (3.1) to the similarity solution for the inner region which is valid at large times. The initial condition is (2.8) with $p = 2$. The similarity solution profile, scaled for $t = 10$, is shown for comparison.

time, while the inner part of the rim grows in a way which suggests a self-similar form. This idea will be developed in Section 4.1.

Finally, solutions to the full strong slip lubrication problem (2.5)-(2.6) have also been computed, also using initial condition (2.8). Here a much longer computational domain, $0 < x < 200$, is necessary, requiring 2000 grid points. In Figure 3.4, we compare the solution at $t = 5$, for $\varepsilon = 0.002$, to the inner and outer solutions. The composite solution (3.13), constructed from the numerical data for the inner and outer solutions, is also shown. It is seen to be a good approximation to the full solution.

4 Large-time behavior: $t \to \infty$

While the derivations in the previous section were carried out for $t = O(1)$, we can hope that the basic distinction of the inner and outer region and that the leading order asymptotics remain valid even for large, but not too large, t. We will therefore investigate the large-time limit

$$t = \frac{\tau}{\delta}, \quad \tau \text{ fixed}, \ \delta \longrightarrow 0, \tag{4.1}$$

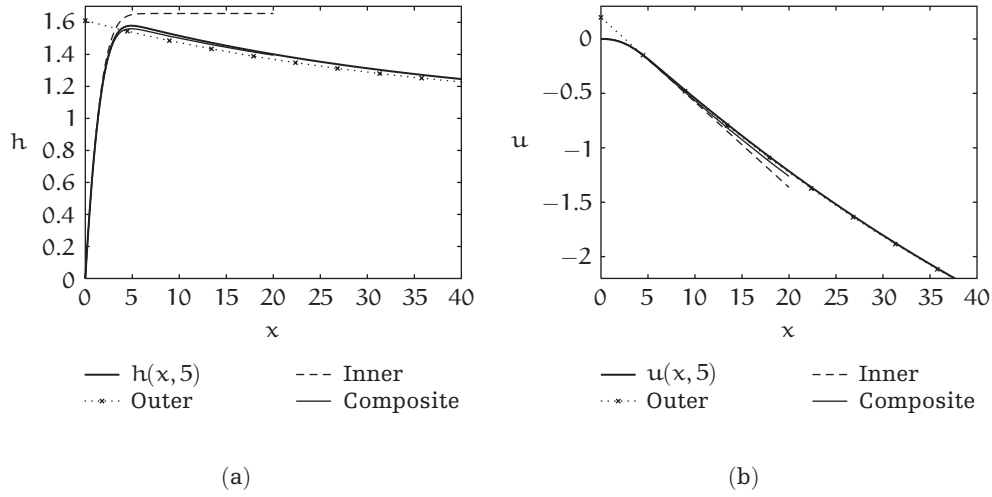

(a) (b)

Figure 3.4 Solution to (2.5) at $t = 5$ for $\varepsilon = 0.002$. (a) h and (b) u. This is compared with the inner solution obtained by integrating (3.1), the outer solution obtained by integrating (3.8), and a composite solution given by (3.13).

separately for the leading order inner and outer problems. As one might expect for initial boundary value problems, the long-time inner and outer solutions approach a form that can be described by one or (in the case of the outer problem) several simple solutions that are largely independent of the initial data. Inspection of the subregions of the outer problem reveals that the result in fact approximates the full problem (2.5)–(2.7) as long as $\delta \gg \varepsilon^{1/2}(\log(1/\varepsilon))^{1/2}$. For δ on the order of this lower bound, one of the subregions of the outer region merges with the inner region (see Section 5).

4.1 Inner problem

First, note that (3.4) implies that $u_0 \sim U_\infty x \sim -x/t$ as $t \to \infty$. Guided by (3.4), we postulate that at large times the behavior of the inner problem (3.1) takes the self-similar form

$$h_0 \sim t\,\eta(\xi) = \delta^{-1}\tau\,\eta(\xi), \quad u_0 \sim \nu(\xi), \tag{4.2}$$

where $\xi = x/t$. Equations (3.1) then become

$$\eta - \xi\eta_\xi + (\nu\,\eta)_\xi = 0, \tag{4.3a}$$

$$4\eta\nu_\xi + \eta\eta_{\xi\xi} - \frac{1}{2}(\eta_\xi)^2 = -\frac{1}{2}\lambda^2. \tag{4.3b}$$

These are subject to the boundary conditions (obtained from (3.3)) at $\xi = 0$,

$$\eta(0) = 0, \qquad \eta_\xi(0) = \lambda, \qquad \eta v_\xi(0) = 0. \tag{4.4}$$

We require that as $\xi \to \infty$, (a) $\eta \to \lambda^2/8$ and (b) $v \sim -\xi$, in agreement with (3.4).

Numerical solutions to this problem have been obtained using a shooting method. By obtaining an expression for ηv_ξ from (4.3b) and substituting this into (4.3a), an expression for v may be found

$$v = \xi - \frac{1}{4\eta_\xi}\left(4\eta + \frac{\eta_\xi^2}{2} - \eta\eta_{\xi\xi} - \frac{\lambda^2}{2}\right). \tag{4.5}$$

The velocity blows up where $\eta = 0$, except for the special case $\eta = \lambda\xi$, which yields $v = 0$. Differentiating to obtain v_ξ, v may be eliminated from (4.3b), yielding a third-order autonomous ODE for η,

$$\eta_{\xi\xi\xi} = \frac{\lambda^2}{2}\left(\frac{\eta_{\xi\xi}}{\eta\eta_\xi} - \frac{\eta_\xi}{\eta^2}\right) - \frac{3}{2}\frac{\eta_\xi\eta_{\xi\xi}}{\eta} + \frac{\eta_{\xi\xi}^2}{\eta_\xi} + \frac{1}{2}\frac{\eta_\xi^3}{\eta^2} - 4\frac{\eta_{\xi\xi}}{\eta_\xi}. \tag{4.6}$$

Note that λ can be eliminated by rescaling.

Given the boundary conditions (4.4), $\xi = 0$ is a singular point. We obtain solutions to (4.6) by integrating from $\xi = \xi_s$ for some small ξ_s, where we assume that the solution locally has the form

$$\eta(\xi) = \lambda\xi + c_1\xi^2 + \cdots. \tag{4.7}$$

Using a shooting method, c_1 is varied until $\eta_\xi = 0$ is satisfied at some point ξ_e sufficiently far from the rim. Taking $\xi_s = 10^{-4}$ and $\xi_e = 5$ is sufficient to obtain well-converged profiles. Figure 4.1 shows the resulting profiles of $\eta(\xi)$ and $v(\xi)$, the latter being found from $\eta(\xi)$ using the relation (4.5) above. The film thickness approaches $1/8$ at large ξ, while $v(\xi) \sim 0.1977 - \xi$, as expected. For these parameters, the required solution has $c_1 = -2.796$. The same solution has been recovered using a boundary value problem solver [15], by imposing $\eta(\xi_1) = 0$, $\eta_\xi(\xi_1) = 1$, and $\eta_\xi(\xi_2) = 0$, and then allowing $\xi_1 \to 0$ and $\xi_2 \to \infty$.

As seen in Figure 3.3, the film thickness in the inner region rapidly approaches the similarity solution, for initial conditions similar to (2.8).

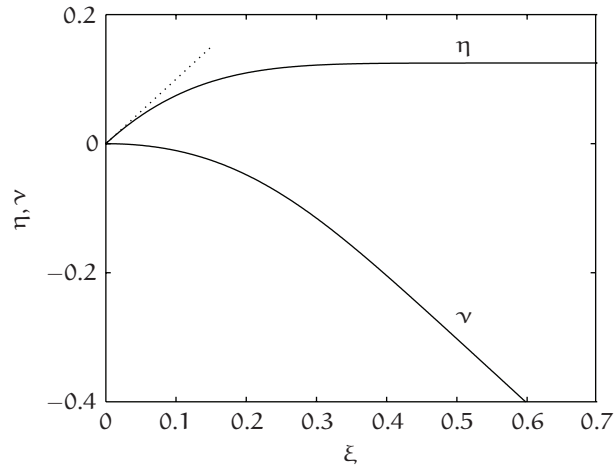

Figure 4.1 The self-similar inner solution found by solving (4.3a) and (4.3b) for $\lambda = 1$. The dashed straight line through the origin has slope λ.

4.2 Outer problem

Now, we examine the outer region, where a more complex structure arises. We study the outer region in three distinct subregions, as shown in Figure 4.2. The asymptotic behavior of $S_0(t)$ remains to be determined from the outer problem, which subdivides into these subregions in the limit $t \to \infty$. Closest to the position of the contact line, we find a solution in a frame moving with the contact line speed, $\dot{S}_0$, denoted the outer left (O1) solution. Most distant from the contact line, a travelling wave solution may be found, which moves with a speed $\dot{\Delta}_0$ relative to the contact line. This is denoted the outer right (O3) solution. An expression for $\Delta_0(t)$, which measures the growing width of the ridge, will be obtained below. Münch and coworkers [2, 11] have shown that the outermost part of the rim is nonoscillatory for small ε (large β) if $\dot{S}$ exceeds an ε-dependent threshold. Finally, between these two "inner" subregions there lies one in which a WKBJ ansatz applies. We refer to this as the O2 subregion. Each of these subregions is described in more detail below.

In the derivations below, we will rescale S_0 and Δ_0 according to

$$S_0 = \frac{1}{\delta\mu} S^*, \qquad \Delta_0 = \mu\Delta^* \tag{4.8}$$

with

$$\mu = \log^{1/2}\left(\frac{1}{\delta}\right), \tag{4.9}$$

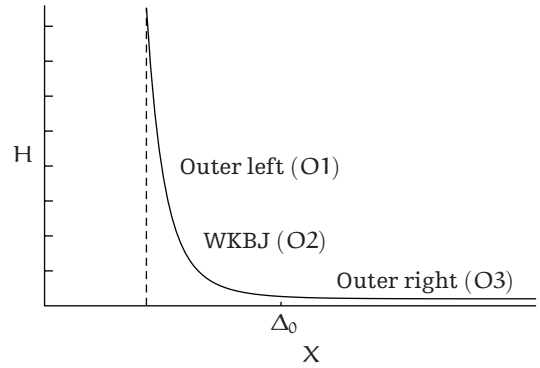

Figure 4.2 At long times ($t \to \infty$), the outer region divides into three subregions.

and assume that S^* and Δ^* are $\mathcal{O}(1)$ for τ fixed and $\delta \to 0^+$. As μ only increases slowly as $\delta \to 0$, this implies a near-linear dependence of S_0 on t and a very slow growth of $\Delta_0(t)$ with t. The justification for these assumptions follows *a posteriori* from the fact that these scalings are those for which the matching of the three subregions succeeds. For a more systematic approach, one could start with a more general ansatz for the scaling factors in (4.8) and then derive the form chosen above in the course of the matching; the current approach benefits from the conciseness with which it can be presented.

4.2.1 Outer right subregion O3. We now consider a "right inner" subregion (most distant from the contact line), in which the profile eventually connects with the unperturbed film, where a travelling wave ansatz is valid. Since we require $h \to 1$ at infinity, a similarity solution for this subregion is unlikely. We introduce a second contact line at $X = \Delta_0(t)$ where the film thickness becomes $\mathcal{O}(1)$. Thus Δ_0 serves as a measure of the width of the rim. (Contrast (3.4), in which H_∞ blows up as $t \to \infty$.) In this subregion, close to Δ_0, we define a new coordinate X_3^* and a new velocity U_3^* by

$$X = \Delta_0 + X_3^*, \qquad U_0 = \dot{\Delta}_0 + \frac{1}{\mu} U_3^*, \tag{4.10}$$

respectively. Indices 1, 2, and 3 refer to the subregion (in this case, O3) to which a variable pertains. After introducing the slow time variable τ and using (4.8), (3.8) reads

$$\delta \frac{\partial H_0}{\partial \tau} + \frac{1}{\mu} \frac{\partial}{\partial X_3^*} \left(U_3^* H_0 \right) = 0, \tag{4.11a}$$

$$4 \frac{\partial}{\partial X_3^*} \left(H_0 \frac{\partial U_3^*}{\partial X_3^*} \right) = S_\tau^* + \delta \mu \Delta_\tau^* + U_3^*, \tag{4.11b}$$

and the boundary conditions (3.10b) become

$$H_0 \longrightarrow 1, \quad U_3^* \longrightarrow -\left(S_\tau^* + \mu\delta\Delta_\tau^*\right) \quad \text{as } X_3^* \longrightarrow \infty. \tag{4.12}$$

After allowing $\delta \to 0$ so that $\delta(\partial H_0/\partial\tau)$ and $\mu\delta\Delta_\tau^*$ may be dropped to leading order from (4.11)-(4.12), (4.11a) may be integrated in X_3^*, yielding

$$U_3^* H_0 = -S_\tau^*, \tag{4.13}$$

after using the boundary conditions (4.12). (Here we make no effort to introduce additional indices for the solution of the leading order problem for (4.11)-(4.12).) Introducing $\sigma(X_3^*) = \log H_0(X_3^*)$, the above equation becomes

$$U_3^* = -S_\tau^* e^{-\sigma}. \tag{4.14}$$

Eliminating U_3^* from (4.11b), multiplying by $d\sigma/dX_3^*$, and integrating results in the first-order ODE,

$$2\left(\frac{d\sigma}{dX_3^*}\right)^2 = \sigma + e^{-\sigma} - 1, \tag{4.15}$$

which can be reduced to a quadrature with the solution satisfying

$$\sigma \longrightarrow 0 \quad \text{as } X_3^* \longrightarrow +\infty. \tag{4.16}$$

This O3 solution is shown in Figure 4.3. This solution blows up as $X_3^* \to -\infty$, as expected if it is to match into a distinct subregion on the left with

$$\sigma \sim \frac{1}{8}\left(-X_3^*\right)^2 + 1 \quad \text{as } X_3^* \longrightarrow -\infty, \tag{4.17}$$

up to translations in X_3^* which we absorb into the definition of Δ_0. The quantity Δ_0 will be fixed by matching to O2.

However, as it stands, this solution cannot match to the inner solution (3.4c)-(3.4d) as it is a travelling wave, with an amplitude which does not increase with time. Therefore, at least one intermediate subregion is needed for matching.

4.2.2 Outer left subregion, O1. Another "inner" subregion (the "outer left" subregion) arises sufficiently close to $X = S_0$. Here we switch to a moving frame with its origin at

$S_0(t)$, defining inner variables X_1^* and U_1^*. We use (4.1), (4.8), and the following scalings:

$$X = \frac{1}{\mu}X_1^*, \qquad H_0 = \frac{1}{\delta}h^*, \qquad U_0 = \frac{\delta}{\mu}U_1^*, \tag{4.18}$$

where the starred quantities are all assumed to be $\mathcal{O}(1)$. Rescaling (3.8) gives

$$\frac{\partial h^*}{\partial \tau} + \frac{\partial}{\partial X_1^*}\left(U_1^* h^*\right) = 0, \tag{4.19a}$$

$$4\mu\frac{\partial}{\partial X_1^*}\left(h^*\frac{\partial U_1^*}{\partial X_1^*}\right) = \frac{\delta}{\mu}U_1^* + \frac{1}{\mu}S_\tau^*. \tag{4.19b}$$

The boundary conditions (3.10a) that arose from matching the inner and outer regions in Section 3 become

$$4h^*\frac{\partial U_1^*}{\partial X_1^*} = -\frac{1}{2}\lambda^2, \quad U_1^* = 0. \tag{4.20}$$

To leading order, the right-hand side of (4.19b) drops out, allowing the resulting equation to be integrated with respect to X_1^* to give

$$4h^*\frac{\partial U_1^*}{\partial X_1^*} = -\frac{1}{2}\lambda^2. \tag{4.21}$$

We use a self-similar ansatz, writing

$$h^* \sim \tau\widehat{H}(X_1^*), \qquad U_1^* \sim \frac{1}{\tau}\widehat{V}(X_1^*), \tag{4.22}$$

and obtain

$$\begin{aligned} &\widehat{H} + (\widehat{V}\widehat{H})_{X_1^*} = 0, \\ &4\widehat{H}\widehat{V}_{X_1^*} = -\frac{1}{2}\lambda^2. \end{aligned} \tag{4.23}$$

The solution of these, subject to the boundary condition $\widehat{V} = 0$ at $X_1^* = 0$ that follows from (4.20), is

$$\widehat{H} = \frac{1}{8}\lambda^2 e^{-AX_1^*}, \qquad \widehat{V} = -\frac{1}{A}\left(e^{AX_1^*} - 1\right), \tag{4.24}$$

which matches with the inner solution (3.4) in the limit $X_1^* \to 0$ (except for the constant term in (3.4c), which becomes insignificant at large t). The new parameter A is fixed by

the mass conservation requirement

$$\widehat{V}\widehat{H} \longrightarrow -S_\tau^* \quad \text{as } X_1^* \longrightarrow \infty. \tag{4.25}$$

(A could also be obtained from the matching process to follow.) Thus, if $A > 0$ so that $\exp(-AX_1^*) \to 0$, then

$$A = \frac{\lambda^2}{8S_\tau^*}; \tag{4.26}$$

this will prove to depend on t only logarithmically.

4.2.3 Outer subregion O2. Finally, to join the two "inner" subregions, we find a solution in the subregion between them. Here we adopt a different scaling, namely,

$$X = \mu X_2^*, \qquad U_0 = \frac{1}{\mu} U_2^*, \tag{4.27}$$

while H_0 is not rescaled. Now, (3.8) reads

$$\delta \frac{\partial H_0}{\partial \tau} + \frac{1}{\mu^2} \frac{\partial}{\partial X_2^*} \left(U_2^* H_0 \right) = 0, \tag{4.28a}$$

$$\frac{4}{\mu^3} \frac{\partial}{\partial X_2^*} \left(H_0 \frac{\partial U_2^*}{\partial X_2^*} \right) = \frac{1}{\mu} U_2^* + \frac{1}{\mu} S_\tau^*. \tag{4.28b}$$

In this subregion, we seek a WKBJ-style approximation via the ansatz

$$\begin{aligned} H_0 &= a_1 \exp\left(\mu^2 \sum_{n=0}^{\infty} \mu^{-2n} G_n\left(X_2^*\right) \right), \\ U_2^* &= -\exp\left(-\mu^2 \sum_{n=0}^{\infty} \mu^{-2n} G_n\left(X_2^*\right) \right), \end{aligned} \tag{4.29}$$

which turns out to be appropriate even though (4.28) is nonlinear. Inserting this ansatz into (4.28), we find that the choice of dominant terms is between the left-hand side of (4.28b) and the second right-hand side term; the term in U_2^* drops out together with the time derivative in (4.28a). Determining the first two terms of the expansion, we obtain

$$H_0 = a_1 \exp\left(\frac{\mu^2 S_\tau^*}{8a_1} {X_2^*}^2 - \frac{a_2}{a_1} X_2^* - \frac{a_3}{a_1} \right), \tag{4.30a}$$

$$U_2^* = -\exp\left(-\frac{\mu^2 S_\tau^*}{8a_1} {X_2^*}^2 + \frac{a_2}{a_1} X_2^* + \frac{a_3}{a_1} \right). \tag{4.30b}$$

The constants a_1, a_2, and a_3 must be found by matching.

4.2.4 Matching. We first match O1 and O2, and then match O2 and O3. The leading terms in the expansion of the O2 solution as $X_2^* \to 0$ are

$$\begin{aligned} H_0 &\sim a_1 \exp\left(-\frac{a_3}{a_1} - \frac{a_2}{a_1} X_2^* \right), \\ U_2^* &\sim -\exp\left(\frac{a_3}{a_1} + \frac{a_2}{a_1} X_2^* \right). \end{aligned} \tag{4.31}$$

The expansion of the O1 solution as $X_1^* \to \infty$ is, when rewritten in O2 variables,

$$\begin{aligned} h^*\left(\mu^2 X_2^*\right) &= \frac{\lambda^2 \tau}{8} \exp\left(-A\mu^2 X_2^* \right), \\ U_1^*\left(\mu^2 X_2^*\right) &\sim -\frac{1}{A\tau} \exp\left(A\mu^2 X_2^* \right). \end{aligned} \tag{4.32}$$

Matching O2 with O1 therefore requires

$$a_1 = \frac{\lambda^2}{8A}, \qquad \frac{a_2}{a_1} = \mu^2 A, \qquad \frac{a_3}{a_1} = \log\left(\frac{\delta}{A\tau} \right), \tag{4.33}$$

and so in the O2 subregion we have from (4.30), and using (4.26),

$$H_0 = \frac{\lambda^2 \tau}{8\delta} \exp\left(\frac{\mu^2 {X_2^*}^2}{8} - \frac{\mu^2 \lambda^2}{8 S_\tau^*} X_2^* \right), \tag{4.34a}$$

$$U_2^* = -\frac{8 S_\tau^* \delta}{\lambda^2 \tau} \exp\left(-\frac{\mu^2 {X_2^*}^2}{8} + \frac{\mu^2 \lambda^2}{8 S_\tau^*} X_2^* \right). \tag{4.34b}$$

It remains to match (4.34) with the solution from the O3 subregion. From (4.10), (4.8), and (4.27), we obtain

$$X_3^* = \mu\left(X_2^* - \Delta^* \right), \tag{4.35}$$

which we insert into (4.17) to express in O2 variables the $X_3^* \to -\infty$ limit of the O3 solution for H_0. We obtain

$$H_0 \sim \exp\left(\frac{\mu^2}{8} \left(X_2^* - \Delta^* \right)^2 + 1 \right). \tag{4.36}$$

Comparison of the above with (4.34a) immediately implies

$$\Delta^* = \frac{\lambda^2}{2S_\tau^*}, \tag{4.37}$$

$$\frac{\lambda^2 \tau}{8\delta} = \exp\left(\frac{\mu^2 \left(\Delta^*\right)^2}{8} + 1\right), \tag{4.38}$$

to match H. Matching U_2^* with U_1^* yields the same conditions as (4.37) and (4.38).

Inserting (4.37) into (4.38) and solving for S_τ^* yield

$$S_\tau^* = \frac{\mu\lambda^2}{4\sqrt{2}}\left(\log\left(\frac{\lambda^2\tau}{8\delta}\right) - 1\right)^{-1/2}. \tag{4.39}$$

In terms of the variables S_0, Δ_0, and t, the expressions (4.37) and (4.39) become

$$\dot{S}_0 = \frac{\lambda^2}{4\sqrt{2}}\left(\log\left(\frac{\lambda^2 t}{8}\right) - 1\right)^{-1/2}, \qquad \Delta_0 = \frac{\lambda^2}{2\dot{S}_0} \tag{4.40}$$

for $t \to \infty$. The expression for $\dot{S}_0$ is not integrable directly but since $\dot{S}_0 \sim \log^{-1/2} t$, it follows that

$$S_0 \sim \frac{\lambda^2 t}{4\sqrt{2}\log^{1/2} t}, \qquad \Delta_0 \sim 2\sqrt{2}\log^{1/2} t. \tag{4.41}$$

Thus, as is to be expected, the dewetting rate increases with the contact angle λ; the manner in which this rate is selected by the asymptotics is somewhat subtle.

4.3 Composite solution and numerical verification

We first compare the solutions for the subregions with numerical simulations for the outer solution $H_0(x,t)$ of (3.8)–(3.11), obtaining good agreement as $t \to \infty$. Numerical simulations for the outer problem were carried out to large times. The speed of the contact line $\dot{S}_0$ obtained from the outer solution is compared to the asymptotic expression (4.40) in Figure 4.4 (line labelled "Outer"). At relatively large times, the outer solution demonstrates a dewetting rate close to that predicted from asymptotic matching. Profiles of the outer solution are shown at various times in Figure 3.2, revealing the increasingly-curved structure which develops at large times, as expected from the theory of Section 4.2. Profiles at $t = 100$ and $t = 10000$ are shown again in Figure 4.3, together with the velocity, where they are compared to the O1 solution and the O3 travelling wave solution. The O3 solution is a credible approximation to the outer profile at these times

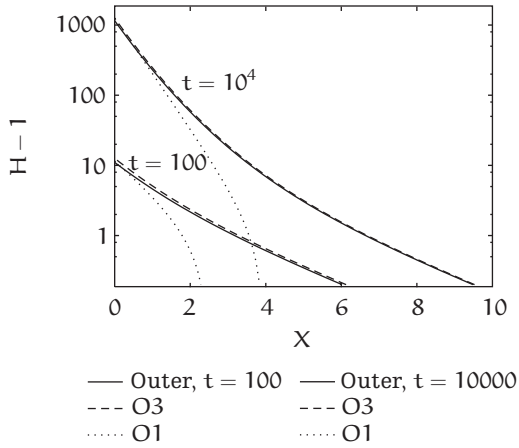

(a)

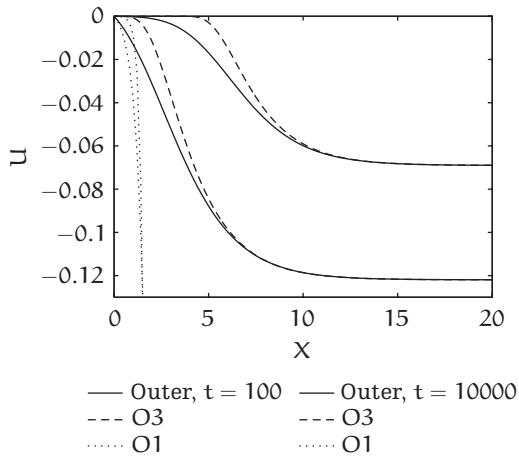

(b)

Figure 4.3 Comparison of outer solution (a) thickness profile $H(X, t_k)$ and (b) velocity $u(X, t_k)$ at $t_k = 100$ and 10000. These are compared to the O1 outer left and O3 outer right solutions at these times, using the value of $\dot{S}_0$ obtained from the outer solution simulation.

for large X, but as expected its accuracy diminishes for small X. Similarly, the O1 solution approximates the outer profile adequately for small X. To see the separation of the outer solution described in Section 4.2 takes quite long times, of order $1/\delta \sim \exp(\mu^2)$. However,

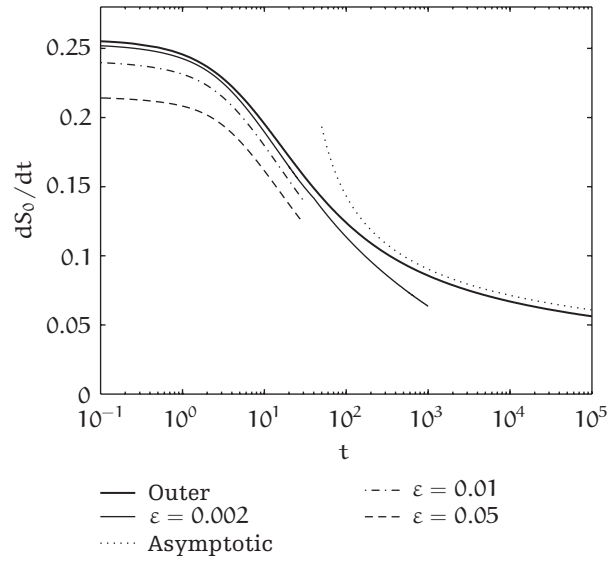

Figure 4.4 Speed $\dot{S}_0(t)$ as predicted using numerical simulations of the outer problem, (3.8), labelled "Outer," and as obtained from the full lubrication model (2.5) with $\varepsilon = 0.05$, $\varepsilon = 0.01$, and $\varepsilon = 0.002$. These are compared to the large-time prediction from matching the outer subregions, (4.40), shown by a dotted line.

in long-time simulations of the outer problem this separation does appear to be visible. (In preparing Figure 4.3, the value of $\dot{S}$ used is taken from the outer simulation so that this is not a completely independent check of the results.) In principle, a composite approximation to the outer solution could be constructed from the asymptotic results for the three subregions. However, we do not attempt to do this here.

We also compare $\dot{S}$ obtained from solutions of the full lubrication model (2.5)–(2.7) with the outer solution. Figure 4.4 shows $\dot{S}$ from simulations for several values of ε, confirming that as ε is reduced, the dewetting rate of the outer solution is approached. However at larger times, the full lubrication model dewetting rates deviate due to the presence of the inner region. This transition to a new time regime is discussed further in the following section. Evidently, at large times (4.40) only approximates the dewetting rates obtained from the full model well for ε even smaller than shown here. For solutions of the full lubrication model to clearly display the separation of the outer region into subregions, this separation must happen before the expanding inner region overtakes the shrinking O1 one and we arrive in Phase 2, discussed below. Finally, we note that

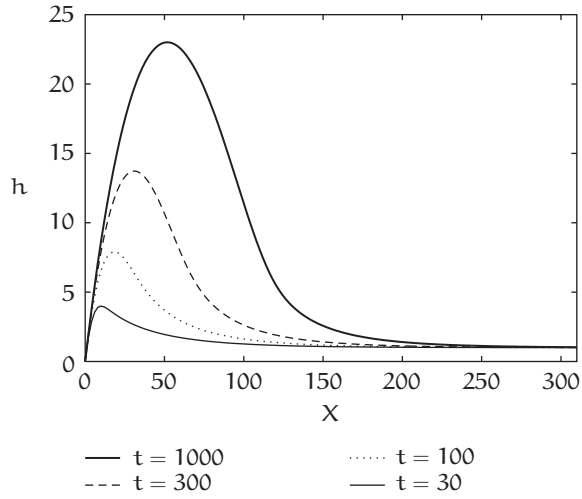

Figure 5.1 Solution of (2.5) for $\varepsilon = 0.002$ at moderately large times. The rim begins to adopt a more symmetric shape.

a composite of the inner and outer solutions may be constructed using (3.13) just as in Section 3.

5 The next time scale, $t = \mathcal{O}(\varepsilon^{-1/2}\log(1/\varepsilon)^{-1/2})$

In the above, the inner region length scale is $x = \mathcal{O}(t)$, whereas the O1 subregion has $x = \mathcal{O}(\varepsilon^{-1/2}/\log^{1/2} t)$. Thus we expect the next time scale to have

$$t = \mathcal{O}\left(\frac{\varepsilon^{-1/2}}{\log^{1/2}\left(\dfrac{1}{\varepsilon}\right)}\right) \tag{5.1}$$

(for small ε), this being the one on which these two length scales merge. In this time scale, we expect that the old O1 and inner regions have merged to form a single new inner region. This inner region coexists with the old O2 and O3 subregions at least until, on an even longer timescale, further changes occur. In this paper, we will not, however, discuss this time regime, or the ones that follow it, in detail.

Figure 5.1 shows the solutions of (2.5) for $\varepsilon = 0.002$ at relatively large times, $30 < t < 1000$. The first of these is a sufficiently late time that the film has entered the second time regime. These rim profiles are in sharp contrast to those found for the outer problem (Figure 3.2), which lack any inner region, and those found at earlier times for the same ε (Figure 3.4).

It is striking that the rim profile on this time scale is of the same parabolic form as the very weak slip one, but the decay towards the precursor film thickness is monotonic in this case but oscillatory (associated with capillary ripples) in the latter.

Here $\varepsilon = 0.002$ so that $t_2 = \varepsilon^{-1/2} \log^{-1/2}(1/\varepsilon) = 8.97$. For the small values of ε encountered in previous numerical studies [11], smaller values of ε are used, and the time required to enter the second phase increases only slowly with ε, reaching $t_2 = 290$ for $\varepsilon = 8.3 \times 10^{-7}$. Thus study of the later time regimes will be important for understanding of physical experiments, which continue to even larger times.

6 Summary

We have shown how the evolution of a dewetting rim with strong slip features a complicated structure, which evolves to form an inner and an outer region. Only in the inner region is surface tension of significance. We found the (sufficiently) long-time limit of the inner region described by a self-similar profile. We computed the evolution of the outer region and demonstrated that, at sufficiently long times, a three-fold structure emerges. At longer times, the growing inner region will modify the spatial structure described here. A detailed discussion of this process will be the subject of future work.

The model discussed here has been limited to one-dimensional dewetting. The issue of transverse instability (or azimuthal instability for circular holes) for the strong slip model would be of interest in the future. The axisymmetric case should also be investigated for possible differences in behavior at relatively early times.

We conclude by remarking that this evolution through a variety of distinct timescales results in the presence of a number of distinct intermediate-asymptotic descriptions of the evolution, one of which (comprising four regions) we have elaborated upon here. As is typical, these intermediate-asymptotic characterizations manifest themselves only over suitable windows in time and are accordingly difficult to capture numerically; the agreement that we have obtained between numerics and asymptotics is therefore encouraging.

Appendix

Computing the full and outer solutions

Here we outline the method used to compute solutions to the full strong slip lubrication model problem (2.2), in a front-moving frame where $z = x - \dot{s}$, that is, (2.5). This is very similar to that used for the outer problem, (3.8)–(3.10), in a front-moving frame; where the outer solution computation differs, we point this out below.

We define a mesh z_i with $N-1$ interior points, so $0 = z_1 < z_2 < \cdots < z_N < z_{N+1} = Z_e$. Here Z_e is some large number, which may be increased as the profile broadens. Approximations $\widehat{h}_i$ and $\widehat{u}_i$ to the true solution at each mesh point are defined, together with an additional unknown $\dot{s}$. These are $2N+3$ unknowns; the necessary equations are obtained as follows.

(i) Discretize the continuity (2.5a) at grid points $i = 2, \ldots, N$ and time $t = t_{k+1}$, using a backward difference for $\partial h/\partial t$ and centered differences in x. ($N-1$ equations.) $\widehat{h}_0 = 0$ is fixed. For the outer problem, $\widehat{h}_0$ is free, but differencing (3.8a) at the leftmost grid point ($i = 1$) gives one additional equation. For the outer problem, *forward* differences in X are used, as U is negative everywhere.

(ii) Discretize (2.5b) or (3.8b) at grid points $i = 2, \ldots, N$, using centered differences in x. Estimates of h_{xxx} at $z_{i\pm 1/2}$ are averaged. ($N-1$ equations; solving these, imposing $\widehat{u}_1 = 0$, and $\widehat{u}_{N+1} = -\dot{s}$ gives $\widehat{u}_2, \ldots, \widehat{u}_N$.) For the outer problem, an estimate of h_{xxx} is not needed.

(iii) Impose $\widehat{h}_{N+1} = 1$ and $\widehat{u}_{N+1} = -\dot{s}$ (for the outer problem, $\widehat{u}_{N+1} = -\dot{S}$) at the right-hand boundary z_{N+1}.

(iv) Impose $\widehat{h}_1 = 0$, $dh/dx = \lambda$ and $\widehat{u}_1 = 0$ at the contact line, z_1. For the outer problem, impose $\widehat{u}_1 = 0$, and $4(h\partial U/\partial X) = -\lambda^2/2$ at z_1 instead.

This yields $2N+1$ ($2N+3$ for the outer problem) nonlinear equations. Notice that H_0 is still free in the outer problem. Of these equations, $(N-1)$ of the velocity unknowns from the interior grid points may be eliminated, and the remaining equations are solved using Matlab's FSOLVE [15].

Mass conservation was checked by evaluating both sides of (3.12) and was found to be acceptable.

Acknowledgments

The first and the third author are supported by Project C10 of the Matheon DFG research centre and, for the third author, a DFG Heisenberg Fellowship, Grant number MU 1626/3-1. The second author thanks the Weierstrass Institute for Applied Analysis and Stochastics (WIAS) for hospitality during a visit to Berlin while this paper was prepared. We thank an anonymous referee for suggestions which improved the organization of the paper.

References

[1] P. Damman, N. Baudelet, and G. Reiter, *Dewetting near the glass transition: transition from a capillary force dominated to a dissipation dominated regime*, Physical Review Letters **91** (2003), no. 21, Article ID 216101, 4 pages.

[2] R. Fetzer, K. Jacobs, A. Münch, B. Wagner, and T. P. Witelski, *New slip regimes and the shape of dewetting thin liquid films*, Physical Review Letters **95** (2005), no. 12, Article ID 127801, 4 pages.

[3] R. Fetzer, M. Rauscher, A. Münch, B. Wagner, and K. Jacobs, *Slip-controlled thin-film dynamics*, Europhysics Letters **75** (2006), no. 4, 638–644.

[4] J. C. Flitton, *Inertia dominated spreading of thin films*, Ph.D. thesis, University of Nottingham, Nottingham, 2001.

[5] K. Kargupta, A. Sharma, and R. Khanna, *Instability, dynamics, and morphology of thin slipping films*, Langmuir **20** (2004), no. 1, 244–253.

[6] J. R. King and M. Bowen, *Moving boundary problems and non-uniqueness for the thin film equation*, European Journal of Applied Mathematics **12** (2001), no. 3, 321–356.

[7] J. R. King, A. Münch, and B. Wagner, *Linear stability of a ridge*, Nonlinearity **19** (2006), no. 12, 2813–2831.

[8] J. R. King and J. M. Oliver, *Thin-film modelling of poroviscous free surface flows*, European Journal of Applied Mathematics **16** (2005), no. 4, 519–553.

[9] E. Lauga, M. P. Brenner, and H. A. Stone, *Microfluidics: the no-slip boundary condition*, Handbook of Experimental Fluid Dynamics (C. Tropea, J. Foss, and A. Yarin, eds.), Springer, New York, in press.

[10] A. Münch and B. Wagner, *Contact-line instability of dewetting thin films*, Physica D **209** (2005), no. 1–4, 178–190.

[11] A. Münch, B. Wagner, and T. P. Witelski, *Lubrication models with small to large slip lengths*, Journal of Engineering Mathematics **53** (2005), no. 3-4, 359–383.

[12] G. Reiter, *Dewetting of highly elastic thin polymer films*, Physical Review Letters **87** (2001), no. 18, Article ID 186101, 4 pages.

[13] G. Reiter, M. Sferrazza, and P. Damman, *Dewetting of thin polymer films at temperatures close to the glass transition*, The European Physical Journal E - Soft Matter **12** (2003), no. 1, 133–138.

[14] T. Vilmin and E. Raphaël, *Dewetting of thin viscoelastic polymer films on slippery substrates*, Europhysics Letters **72** (2005), no. 5, 781–787.

[15] The MathWorks, Natick, Massachusetts. *MATLAB version 7.0.0.19901 (computer software)*, 2004.

P. L. Evans: Institute of Mathematics, Humboldt University of Berlin, Unter den Linden 6,
10099 Berlin, Germany
E-mail address: pevans@mathematik.hu-berlin.de

J. R. King: School of Mathematical Sciences, University of Nottingham, Nottingham NG7 2RD, UK
E-mail address: john.king@nottingham.ac.uk

A. Münch: Institute of Mathematics, Humboldt University of Berlin, Unter den Linden 6,
10099 Berlin, Germany
E-mail address: muench@mathematik.hu-berlin.de